LHCb-PUB-2014-003
March 25, 2014

The digitisation of the scintillating fibre detector

E. Cogneras[1], M. Martinelli[2], J. van Tilburg[2], J. de Vries[2].

[1] *Clermont Université, Université Blaise Pascal, CNRS/IN2P3, LPC, Clermont-Ferrand, France*
[2] *Nikhef National Institute for Subatomic Physics, Amsterdam, The Netherlands*

Abstract

In this note the digitisation of the scintillating fibre detector for the LHCb upgrade is described. The steps for transforming the hits generated by the GEANT simulation into a digital signal are given. The main effects of this detector are described in the simulation code for the LHCb upgrade. In particular, the attenuation of the fibres after irradiation, the geometry of the fibres with respect to the SiPM channels, the gain of the SiPM's, the thermal noise, the noise from afterpulses and spillover, and the clustering are described. The output is given in the same data format as the one that is expected from the final detector.

1 Introduction

The electronic response of the scintillating fibre detector has been implemented in the simulation software for the LHCb upgrade studies. The aim of this digitisation is to simulate in the effects from the fibres, the SiPM's and the front-end electronics. In particular the following effects are simulated:

- Light yield of the fibres in term of photons.
- Attenuation of the light in the fibres (after irradiation) and the reflection at one end of the fibre.
- The geometric coupling of the fibres to the SiPM channels.
- Gain of the SiPM's in terms of photo-electrons (PE's) and ADC counts.
- The thermal noise and the noise from afterpulses and spillover.
- The clustering algorithm that is implemented in the front-end electronics.
- The encoding and decoding of the data format (banks) from the TELL40.

These items and their effects on the track reconstruction will be discussed in this note. The geometry of the scintillating fibre detector is described in another note [1]. The final track reconstruction is discussed in Ref. [2] and [3].

2 Description of the fibres

The response of fibres is described in terms of the light yield of the fibres, the light attenuation of the light in the fibres (after irradiation), the reflection at one end of the fibre and the geometric coupling of the fibres to the SiPM channels.

2.1 From hit position to channel

In the geometry description [1] the individual fibres are not described. The smallest elements are the fibre mats. For this reason the Geant simulation [4, 5] generates only the entry and exit points of the particles with the fibre mats. These Geant hits are the input for the digitisation. Since the fibres are not aligned with the SiPM channels there is no attempt to describe the location of the individual fibres. Hence, the hit positions are directly converted to channels. This is done by converting the hit positions in the global coordinate system to the local coordinate system corresponding to the detector layer. In this way the vertical and stereo layers are correctly described. Within one quarter the SiPM numbering goes from 0 to 97, for positive x increasing with x, while for negative x decreasing with x. A SiPM consists of 128 channels of 0.25 mm each. In the middle of each SiPM there is a small gap of one channel wide. Between the SiPM's a gap of 0.50 mm

Variable	λ_{short}	λ_{long}	F_s	C_R
Value	200 mm	4700 mm	0.18	0.7

Table 1: List of parameters used to simulate the signal attenuation through the scintillating fibers, and their default value.

is simulated. The channel numbering goes from 0 to 128 always increasing in the direction of increasing x.

For each channel that is hit the fractional position of the entry and exit points is determined. This number is in the range $[-0.5, 0.5]$ such that channels in the middle of a cluster will have fractional position equal to zero. This is used to determine the light sharing between neighbouring channels. The light sharing describes the effect of the staggering and the non-alignment of the fibres with respect to the channels. The fraction of the light going to the right channel is given by

$$f_{\text{right}} = \begin{cases} 0.32\,p + 0.16 & \text{for } p < 0 \\ 0.68\,p + 0.16 & \text{for } p > 0\ , \end{cases} \tag{1}$$

where p is the fractional position. The light going to the left channel, f_{left}, is symmetric. The fraction of the total energy is then given by the fraction of the path length through that channel and the light sharing fraction. The total energy is taken from the Geant hit.

2.2 Simulation of the fiber response

The attenuation factor of the light generated in the fibres is given by

$$a(l) = F_S\, e^{-(\frac{l}{\lambda_{short}})} + (1 - F_S)\, e^{-(\frac{l}{\lambda_{long}})} \tag{2}$$

where l defines the path length through the fibre, λ_{short} and λ_{long} the attenuation length of the short and long components and F_S the contribution of the short attenuation. The corresponding values are reported in Table 1. A mirror at the $y = 0$ end of the fibres reflects the light back to the SiPM's. The reflection coefficient C_R is given in Table 1. The reflected light has a larger attenuation and also arrives a little later than the original pulse.

The effect of the irradiation of the fibres has also to be considered. The attenuation length of fibre is a decreasing function of the irradiation dose. The closer the fibre is to the beam pipe, the more radiation it receives, leading to a negative gradient of the attenuation length towards the beam pipe. Considering the worst case, after 50 fb^{-1} of collected data, the most irradiated region has a diamond shape whose attenuation factor in one quadrant is represented in Fig. 1. The attenuation maps for the direct signal and the reflected signal are given in Fig. 2 as a function of the (x, y) coordinates of the hit.

After this first step of the digitization process it is found that

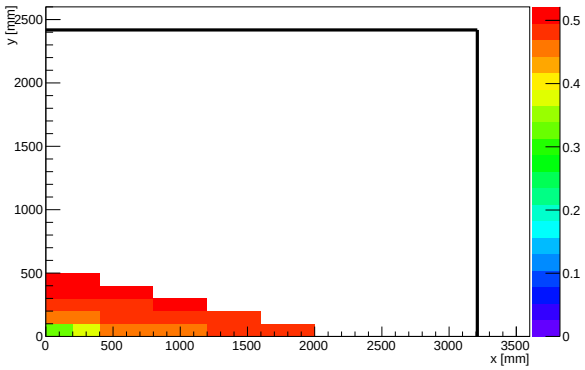

Figure 1: Correction factor obtained from the gradient of attenuation length associated to the fiber irradiation damage after 50 fb^{-1} of collected data. Black lines represent the edges of the layer.

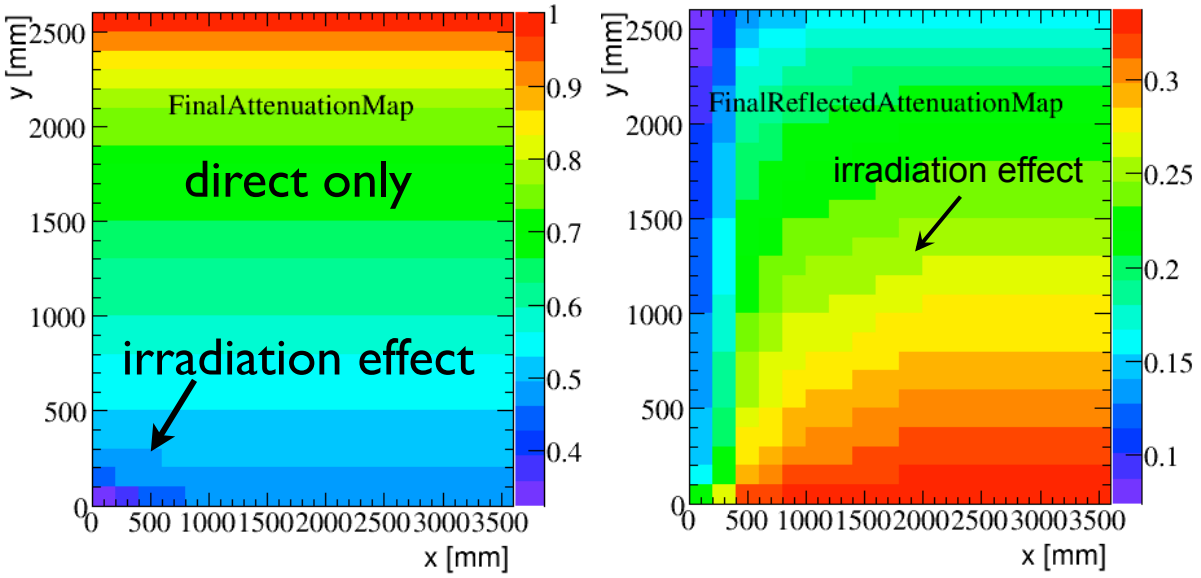

Figure 2: Correction factor applied to the hit energy as a function of the hit position in one quarter of a fiber layer. The plot on the left shows the effect of the scintillating fiber attenuation length on signal reaching directly the SiPM whereas the plot on the right gives the correction factor applied on the signal reflected by the fiber mirrors. Both figures include the fibre irradiation damage after 50 fb^{-1} of collected data.

- in most of cases, a hit deposits its energy in less than 8 SiPM-channels (c.f. Fig. 3 (a). This provides a constraint on the clustering algorithm, described in Sect. 5, which can limit the width of the reconstructed clusters to 8.
- in most of cases, a SiPM-channel has only 1 Geant hit as shown in Fig. 3 (b).

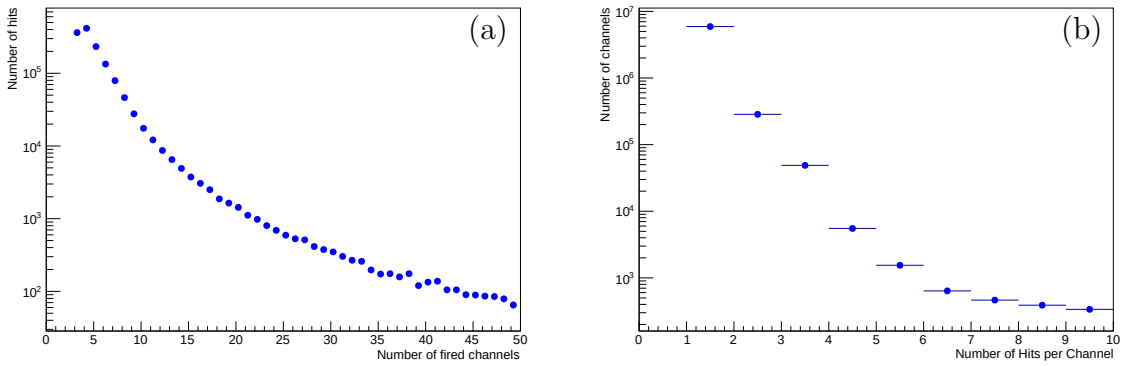

Figure 3: (a) Distribution of the number of fired SiPM-channels per Geant hit. (b) Number of hits per fired SiPM-channel.

3 Simulation of the SiPM response

The next step consists in converting the deposited energy of each channel into photo-electrons. Figure 4 (a) shows the distribution of the energy deposited by the Geant hits. One can see that a MIP corresponds to about 0.2 MeV. Assuming that the SiPM creates 25 photoelectrons per MIP, the number of photo-electrons per MeV is set to 120. An integer number of photo-electrons is drawn from a Poisson distribution.

The number of photo-electrons is then converted into a 6-bit ADC number. A gain factor of 2.0 ADC counts per photo-electron is used. This factor includes both the gain from the SiPM and the analog to digital transfer function. The default value of this parameter is chosen to get in the end a mean cluster charge of around 50 ADC counts.

To simulate the random behaviour of this analog to digital transfer function, the gain factor is modulated according to a Gaussian distribution with a width equal to 5% of the gain factor. Finally, the electronic noise of SiPM is added, which is simulated by a Gaussian with a width of 0.5 ADC counts.

Figure 4 (b) shows a 2D-plot of the ADC counts as a function of the energy deposited in SiPM channel. The light blue curve represents the mean ADC value per energy bin, whose linear fit is given by the red line. The slope is equal to 224.88 ADC/ MeV, roughly corresponding to the number of photo-electrons per MIP multiplied with the gain. Table 2 gives an overview of the parameters used for converting the energy into ADC counts.

3.1 Time description

The time of arrival of the photons at the SiPM is composed of

$$t_{\mathrm{SiPM}} = t_{\mathrm{spill}} + t_{\mathrm{flight}} + t_{\mathrm{scint}} + t_{\mathrm{prop}} \ , \tag{3}$$

where t_{spill} is the time of the bunch crossing, which is -50 ns, -25 ns, 0 ns, 25 ns or 50 ns in the current simulation, t_{flight} is the time of flight of the particle from the pp interaction

Variable	Value
Photo-electrons per MeV	120
Gain of the SiPM per photo-electron	2.0 ADC
Relative variation in the SiPM gain	5%
Electronic noise	0.5 ADC

Table 2: List of parameters used to simulate the SiPM response, and their default value.

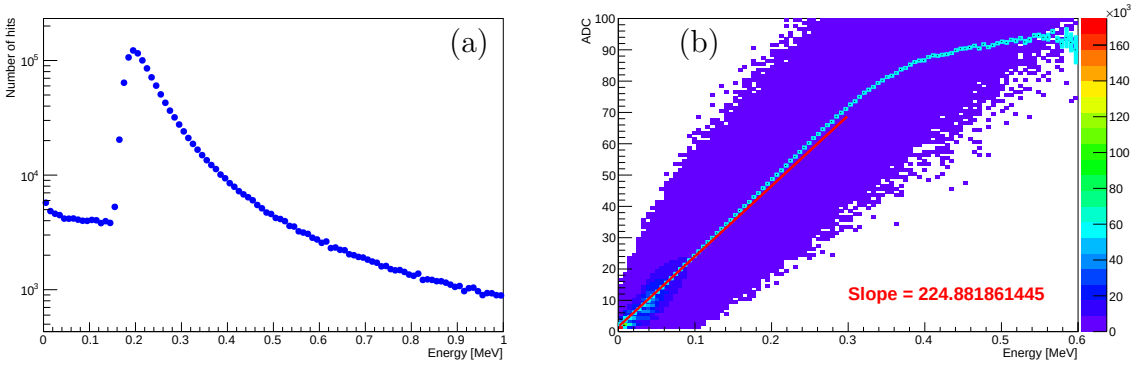

Figure 4: On the left : Distribution of energy deposited by hits. On the right : 2D-plot of ADC counts as a function of the deposited energy. The light blue dots show the mean ADC per bin of energy. The red line is the associated linear fit. The obtained slope is consistent with input parameters.

to the detection plane, t_{scint} is the decay time of the scintillation process, and t_{prop} is the propagation time of the photons through the fibre. After the passage of the particle it takes some time before the scintillation light is released. To determine t_{scint} a random number is drawn from an exponential decay function with a decay time of 2.8 ns. To determine t_{prop}, the propagation time of the light is assumed to be 6.0 ns/ m and the distance from the hit to the SiPM is used. For the reflected photons, the propagation time is always longer because the photons travel first to the mirror-end before traveling the full length of the fibre. Figure 5 shows the number of channels with some deposited energy as function of t_{SiPM}.

The size of the electronic signal that is recorded after the shaper, integrator and ADC conversion on the front-end boards, depends on the time of arrival of the scintillation light at the SiPM. The sampling time of the integrator is chosen to get the largest signal gain for most of the particles. The reflected signal and the signals from previous bunch crossings (i.e. the spillover) will arrive at different times, resulting in lower gains for these contributions. The single pulse response function used in the simulation is shown in Fig. 6.

The sampling time of the integrator is chosen such that the signal height from the current bunch crossing is maximal. This means that a t_0 offset is subtracted from the

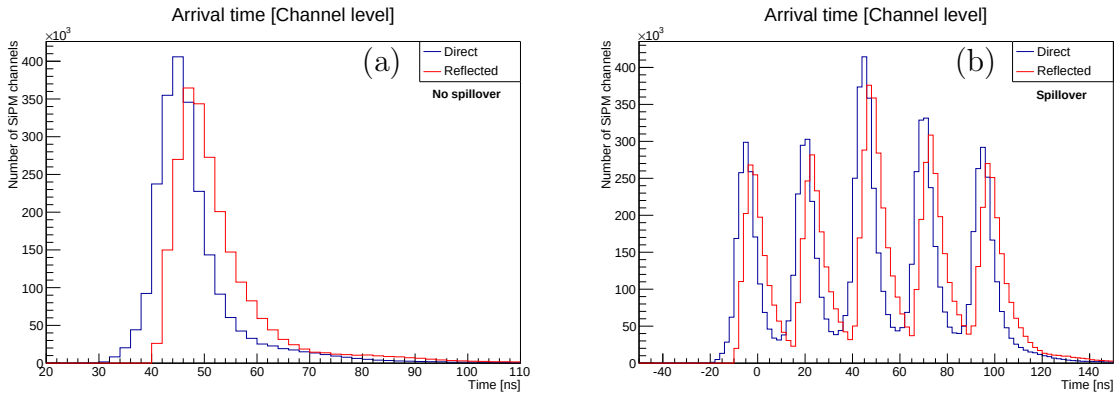

Figure 5: The number of channels with some deposited energy versus the time of arrival at the SiPM (t_{SiPM} for (a) without spillover, and (b) with spillover). No ADC conversion and no clustering is applied at this stage. The five different bunch crossings can be identified; the central peak is the signal spill.

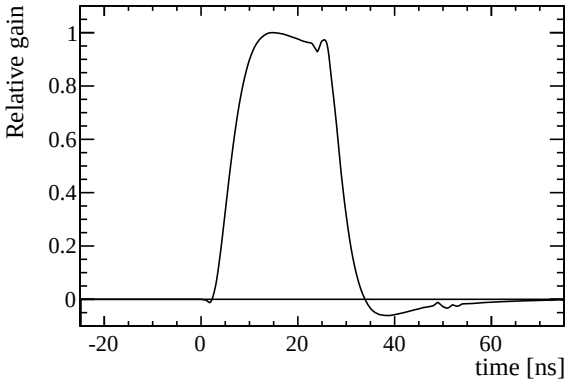

Figure 6: The time response function of the electronics on a single pulse. The arrival time of the pulse at the SiPM is arbitrary.

arrival time at the SiPM,

$$t_{\mathrm{sampling}} = t_{\mathrm{SiPM}} - t_0 \ . \tag{4}$$

As the three stations are located at different z positions, t_0 is set individually for each station. There is a 2 ns difference in t_0 between the stations, as shown in Table 3. The time offset is adjusted such that the sampling time is around 15 ns, which is at the maximum of the response function in Fig. 6.

4 Spillover, thermal noise and afterpulses

Four types of noise can be distinguished:

Station	t_0
T1	21 ns
T2	23 ns
T3	25 ns

Table 3: Time offsets (t_0) for each tracking station.

- Spillover noise, which is charge associated with real hits from previous or next bunch crossings that spill into the current integration window. This is simulated as described in Sect. 3.1.
- Thermal (dark) noise, which is due to thermal fluctuations in the SiPM and depends on temperature and irradiation.
- Afterpulses, which are due to charge carriers being trapped in the SiPM, and released after some time (mostly in following events).
- Cross-talk, which are additional photo-electrons being released in neighbouring pixels due to UV radiation coming from an avalanche in the current pixel.

The effect of cross-talk is basically a charge enlargement on single photo-electrons, since most of the time the neighbouring pixels belong to the same readout channel. Therefore, cross-talk is not considered as an independent source of noise, but rather added to dark noise and afterpulse noise to (statistically) increase the channel charge at the end.

4.1 Thermal noise

Thermal noise depends on the temperature and irradiation of the SiPMs. For the number of channels per event that should receive a thermal noise contribution of one photo-electron, the following relation is used:

$$N_{\text{th}} = N_{\text{ch}} \times \frac{0.1 + 50\left(\int \mathcal{L}\,\mathrm{d}t\right)}{40} \times 2^{\frac{T-20}{10}} \ , \tag{5}$$

where T is the temperature in °C, $\int \mathcal{L}\mathrm{d}t$ is the integrated luminosity in fb^{-1}, and N_{ch} is the total number of channels in the fibre tracker (= 12 layers x 4 quarters x 6 modules x 4 mats x 4 SiPMs x 128 channels). The thermal noise rate per channel at $T = 20\,^{\circ}\mathrm{C}$ increases from 100 kHz at $0\,\mathrm{fb}^{-1}$ to 250 MHz at $50\,\mathrm{fb}^{-1}$. The noise rate increases by a factor of two for every 10 °C. These numbers are obtained from in-situ irradiation studies of the SiPMs [6].

A number of random channels, given by Eq. (5) is chosen to create thermal noise. Since a thermal noise hit typically results in only one photo-electron, most of these noise hits will not be visible after clustering. However, if the noise rate is high enough such that several pixels in one channel or in neighbouring channels fire, then the cluster thresholds

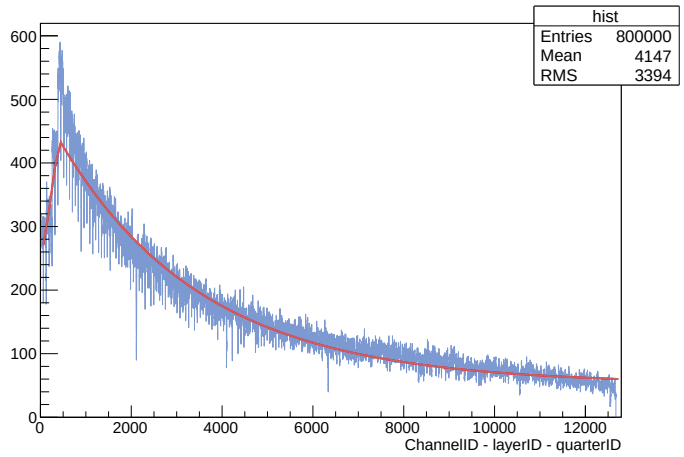

Figure 7: Fit to the channel hit occupancy, all 4x12 quarters added.

can be exceeded, giving rise to noise clusters. In addition, the effect of cross-talk will effectively increase the number of photo-electrons as well. The deposited charge in a given channel is increased by adding photo-electrons with a the cross-talk probability of 7%.

4.2 Hit afterpulses

Afterpulses come from charge carriers being trapped in the SiPM. They are released after some time, which can be many bunch crossing later. Since the afterpulses in the current event can come from many bunch crossings before, it is practically impossible to fully simulate all these spillover events. Instead, the occupancy profile is taken from a fit to the channel hit occupancy as shown in Fig. 7. The fit model is described by an exponentially rising part for channels close to the beam pipe, and falling part described by another exponential, as given by

$$f(x) = \begin{cases} A + N_1 \times e^{a_1 x} & ,(x \leq C) \\ A + (N_1 \frac{e^{a_1 C}}{e^{a_2 C}}) \times e^{a_2 x} & ,(x > C) \end{cases} \tag{6}$$

where x is the channel number and A, N_1, a_1, a_2, C are parameters that are taken from a fit to the occupancy profile in Fig. 7. The parameters and their values are given in Table 4. This shape is then used to draw random channels according to this distribution.

The afterpulse probability depends on the time after the original hit and follows a double exponential with decay constants of 25 ns and 100 ns with equal probabilities. Furthermore, the intensity of the pulse depends on the recovery time of the pixel, resulting in a turn-on. The afterpulse probability as a function of the time after the initial pulse is then given by

$$\mathcal{P}_{\mathrm{AP}}(t) = \mathcal{P}_{\mathrm{AP}}(0) \left(1 - e^{\frac{t}{t_{\mathrm{recovery}}}}\right) \left(f_{\mathrm{slow}} e^{\frac{t}{t_{\mathrm{short}}}} + (1 - f_{\mathrm{slow}}) e^{\frac{t}{t_{\mathrm{long}}}}\right) , \tag{7}$$

Table 4: Result of the fit of Eq. 6 to the channel hit occupancy in Fig. 7.

variable	fit value
N_1	1.96417e+02
C	3.91714e+02
a_1	1.72776e-03
a_2	-3.18658e-04
A	5.25770e+01

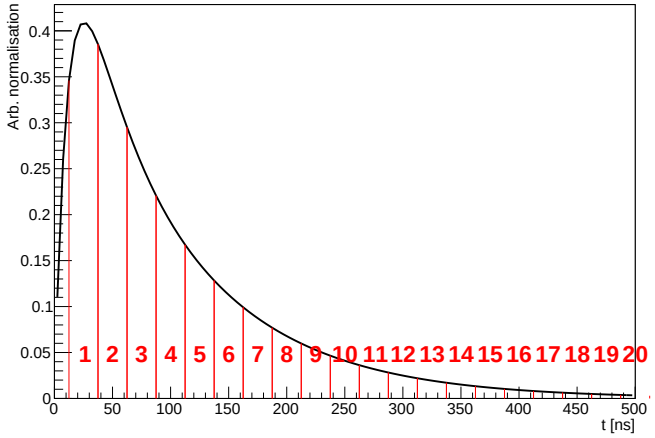

Figure 8: Afterpulse time distribution. The different bunch crossings are numbered and indicated in red. The distribution is not normalised.

where $t_{\text{recovery}} = 20\,\text{ns}$ is the recovery time of the pixel, $t_{\text{short}} = 25\,\text{ns}$ is the short decay constant, $t_{\text{long}} = 100\,\text{ns}$ is the short decay constant, and $f_{\text{short}} = 0.5$ is the contribution of the short component. The shape of the afterpulse probability is shown in Fig. 8.

The integrated afterpulse probability is assumed to be 15% per fired pixel. Since there are many pixels per channel ($\sim$ 80 pixels), each fired pixel will typically correspond to only one photo-electron. This means that in order to create a cluster, several pixels, each with 15% probability, have to afterpulse in the same 25 ns readout window. Therefore, the ADC charge of the afterpulse clusters is much smaller than that of the signal.

The hit afterpulses are simulated as follows. Looping over the average number of clusters per event ($\sim$4k for $\nu = 7.6$), with an additional 16% due to afterpulses on the hit afterpulses, a random number from a Landau distribution obtained from a fit to the cluster charge distribution (Fig. 9) is taken as the number of fired pixels in that channel. Then, the number of afterpulses in this channel is determined from a Poisson distribution with a mean equal to the number of fired pixels multiplied by the afterpulse probability. Each of the afterpulses is then put into a time bin of 25 ns according to the probabilities in Fig. 8. The number of photo-electrons in each time bin is then assigned to a different

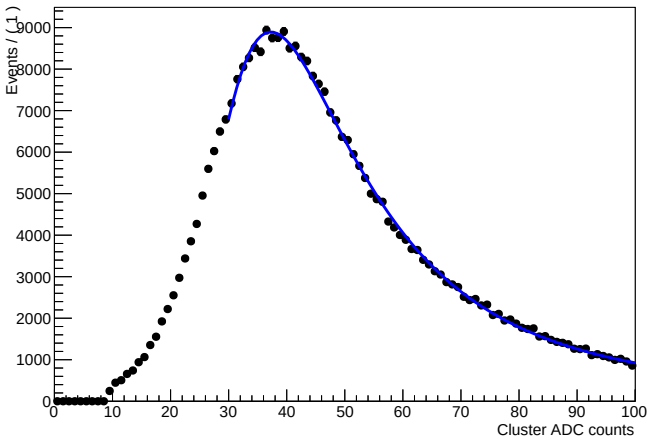

Figure 9: Landau fit to the cluster charge distribution.

random channel, according to the occupancy profile. For each channel, cross-talk is added depending on the number of photo-electrons in the channel. The charge of a channel is not shared among neighbouring channels (the cluster size), which makes a slight overestimation of the noise (since the cluster seeding threshold is exceeded more often). If the same channel is drawn multiple times, the charge is added.

5 Simulation of the electronics

The zero-suppression and clustering is already done on the front-end FPGA's before the data is sent to the TELL40 readout boards. For this reason the clustering algorithm needs to be emulated in the LHCb simulation. The simulated data is converted into a data format of 16-bit words that is sent to the TELL40. In the following these two steps are described.

5.1 Clustering and zero suppression

The clusters of fired channels are searched for by looping over all channels in a SiPM. The steps in the clustering are given below:

1. Once a channel is found to have 1 ADC count or more, this channel is set as the starting channel of a cluster.

2. Each neighbour channel fulfills this requirement is added to the cluster.

3. The cluster ends as soon as the neighbouring channel

    - is below this threshold,

Variable	Value
ADC threshold	1 ADC
Minimum cluster size	1 channel
Maximum cluster size	8 channels
Minimum cluster charge	9 ADC
Minimum charge in highest channel	6 ADC

Table 5: Parameters used in the simulation of the clustering and their default value.

- is the last channel (128^{th}) of the SiPM, or the 64^{th} channel (unsensitive channel located in the middle of the SiPM array).

4. To be kept, a cluster has to pass the following conditions:
   - the size of the cluster has to be at least 1 and at most 8 channels,
   - the total charge of the cluster has to be 9 ADC counts or more, and
   - at least one channel has to have a charge of 6 ADC counts or more.
5. The loop continues with the next channel starting again with step 1.

The clustering parameters can be easily modified and are given in Table 5. With the current settings a cluster efficiency of $\sim 99\%$ is found. For each cluster that is found, three variables are passed through:

- the average channel number of the cluster. The integer part represents a physical channel whereas the fractional part helps to improve the granularity,
- the cluster size, which is the number of SiPM-channels in the cluster, and
- the total cluster charge, which is the sum of ADC counts of all channels in the cluster.

5.2 Data format

The data are optically sent from the frond-end electronics to TELL40 readout boards through GBT cards [7] whose transfer rate is limited to 3.2 Gb/ s. The encoding of the clusters in the corresponding data format is emulated in the LHCb simulation. To read again the raw data for the track reconstruction the decoding of the clusters is also implemented. As shown in Fig. 10, the data format consists of a 16-bits header divided into three parts: a 12-bit bunch crossing ID (BCID), one truncation bit and 3 bits for the number of clusters in the SiPM. This means that the number of clusters in a 128-channel SiPM is limited to 8. After the header the information of the clusters follows. Each cluster consists of 16 bits, of which 4 bits are for the cluster charge, 3 bits for the cluster size, 7 bits for the channel number, and 2 bits for the fractional part.

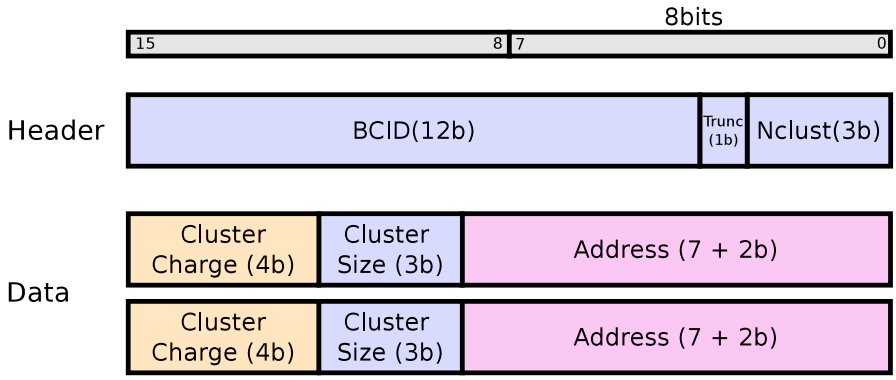

Figure 10: Format of data from GBT cards to TELL40 readout board.

6 Results

This section gives the cluster distributions of the simulation and the performance of the track reconstruction. For these studies a sample of 100 $B_s^0 \to \phi\phi$ simulated events is used, with $\nu = 7.6$.

6.1 Cluster position

Figure 11 shows the spatial distribution in x and y of the hits that result in clusters. As each station and layer exhibit a similar distribution[1], all layers are overlaid in this figure. As expected the highest flux of particles is seen close to the beam pipe.

6.2 Thermal noise and afterpulsing

Clusters from thermal noise and afterpulses are expected to give smaller clusters and with lower charge compared to signal clusters. The cluster charge and size for signal and thermal noise at $T = -30\,°\mathrm{C}$ can be seen in Fig. 12. The signal clusters are typically three channels wide, while the noise clusters are typically two channels wide. The cluster charge and size for afterpulses can be seen in Fig. 13. The cluster size distribution for afterpulses peaks at one. The cluster charge for both thermal noise and afterpulses peaks at low ADC values and can be easily reduced by increasing the clustering thresholds at the cost of clustering efficiency.

The occupancy of clusters at the SiPM for signal, thermal noise at $T = -30\,°\mathrm{C}$ and afterpulses is shown in Fig. 14. In the hottest regions, there are 3.5 clusters per SiPM

[1]Ignoring slight differences caused by the increasing radius of the beampipe along z or shadowing of the magnet.

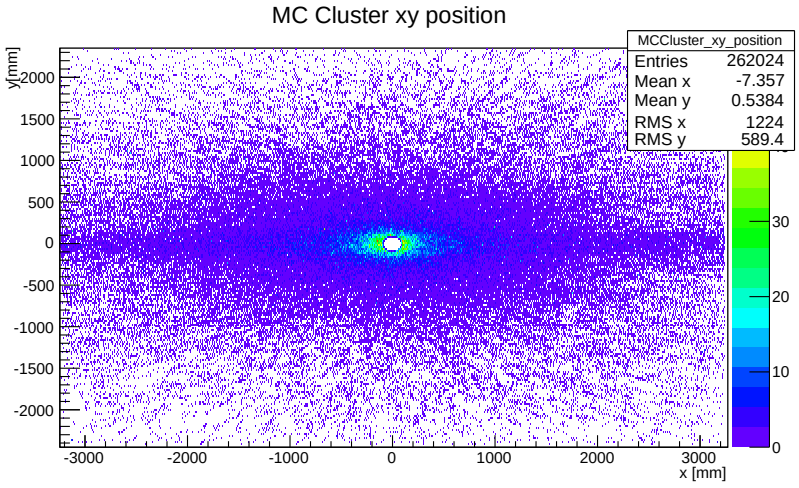

Figure 11: Spatial position (x, y) of the clusters in all stations.

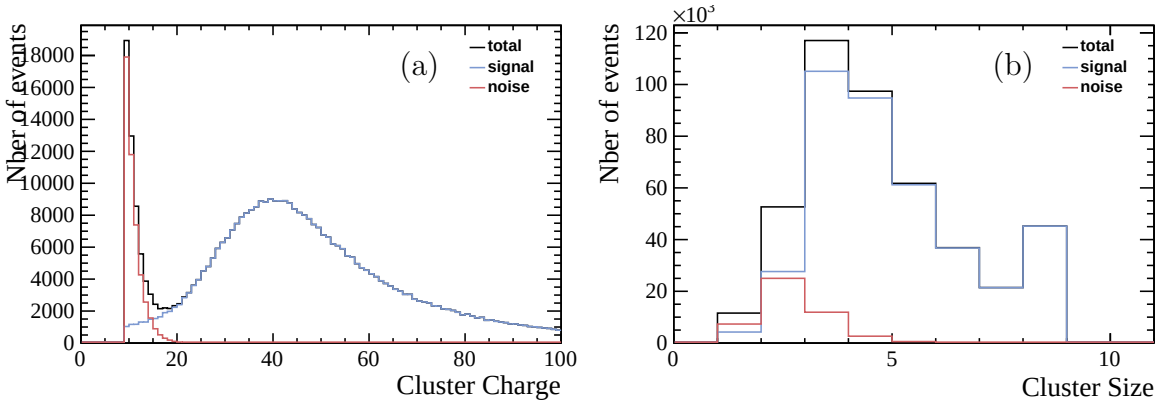

Figure 12: (a) Total charge of the clusters in terms of ADC counts and (b) cluster size in numbers of channels for signal clusters (blue), thermal noise (red) and both (black) at $T = -30\,^{\circ}\mathrm{C}$.

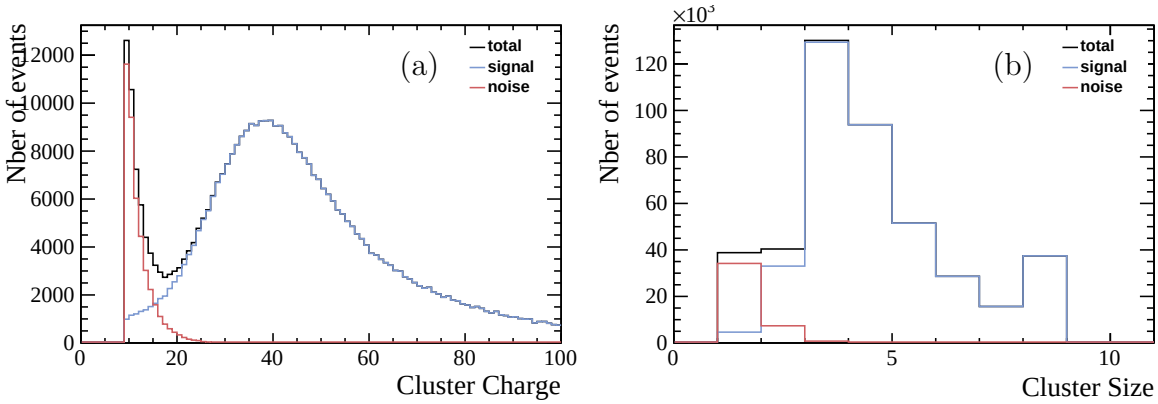

Figure 13: (a) Total charge of the clusters in terms of ADC counts and (b) cluster size in numbers of channels for signal clusters (blue), afterpulses (red) and both (black).

(128 channels), while in the outer regions, the occupancy is more than a factor 10 lower. As expected the occupancy of the thermal noise is flat along the detector channels. On average every SiPM sends out 0.1 thermal noise cluster every event at $T = -30\,^{\circ}\mathrm{C}$. For the afterpulses, the occupancy profile follows that of the signal. There are about 10 times less afterpulses than signal clusters. This results in less than 0.4 afterpulses per SiPM even in the hottest regions of the detector.

6.3 Spillover

The number of spillover clusters amounts to about 10% of the number of signal clusters. This fraction depends strongly on the electronic response function as shown in Fig. 6 and will become larger in case the integration time becomes longer. The cluster charge in ADC counts is shown for signal and spillover clusters in Fig. 15 (a). The average charge for spillover clusters is slightly lower compared to that of the signal clusters. The cluster size

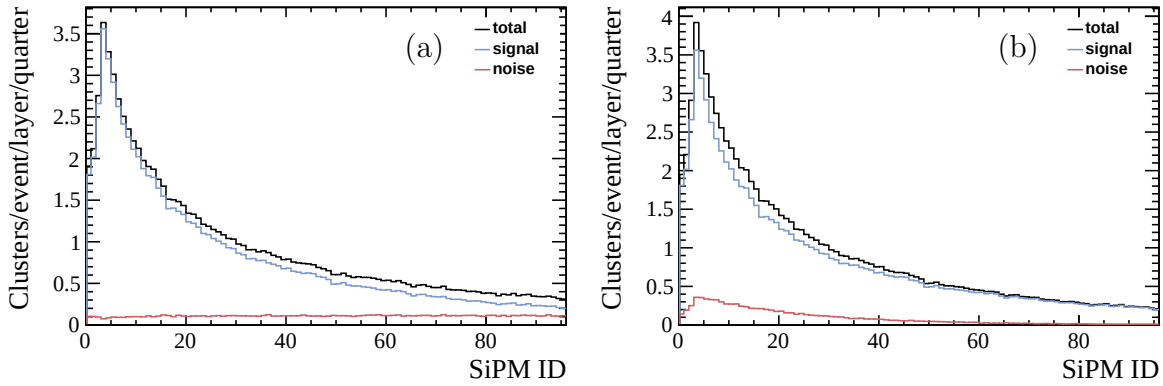

Figure 14: (a) Occupancy of clusters at the SiPMs for signal and thermal noise at $T = -30\,^{\circ}\mathrm{C}$ (red) and (b) for signal and afterpulses.

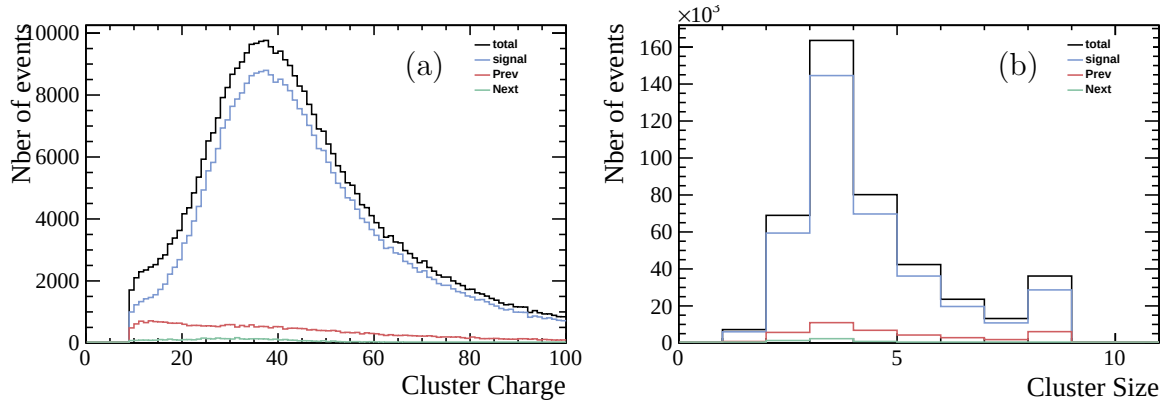

Figure 15: (a) Total charge of the clusters in terms of ADC counts and (b) cluster size in numbers of channels for signal and spillover.

is slightly larger for spillover clusters compared to signal clusters as can be seen in Fig. 15 (b). Figure 16 shows the SiPM position of the spillover clusters and Fig. 17 shows the y position of the Geant hits from which the cluster originates. The spillover clusters are distributed more towards higher x and higher y positions compared to signal clusters. The main contribution comes from slow (low momentum and often secondary) particles from the previous bunch crossing that are distributed more towards the outside of the detector due to the magnetic field. Also (fast) particles from the next bunch crossing contribute. These are mainly particles in the region around the beam pipe and particles at large y positions as their scintillation light does not have to travel through the whole fibre. Close to the SiPM readout, i.e. for $|y| \gtrsim 2000\,\mathrm{mm}$, the number of spillover clusters is almost as large as the number of signal clusters.

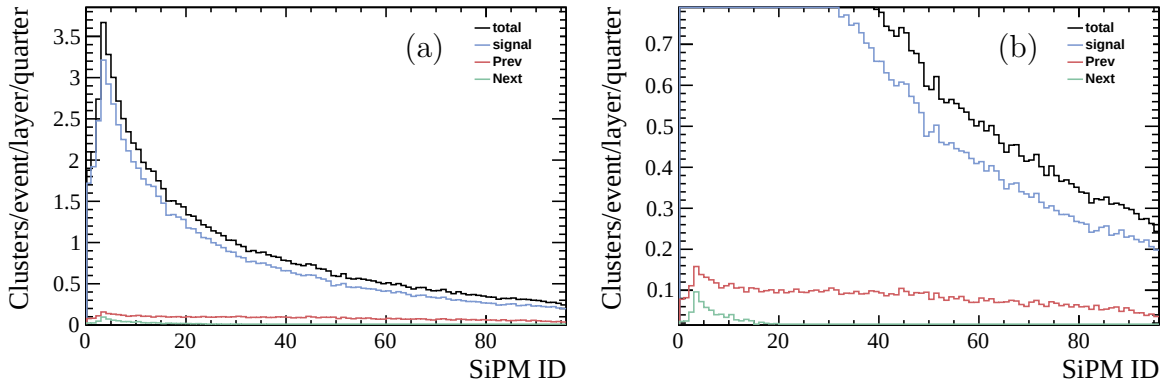

Figure 16: (a) Occupancy of clusters at the SiPM and (b) a zoom to see the spillover profile.

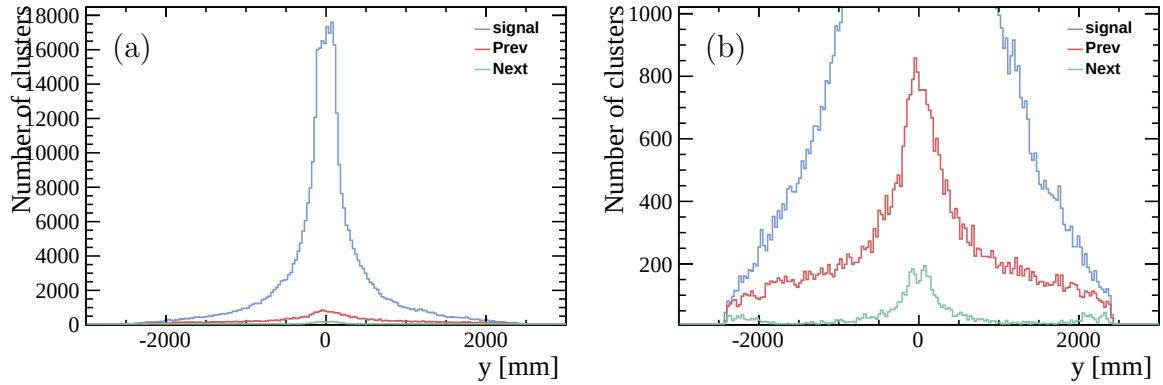

Figure 17: (a) The y position of the MC hit resulting in a cluster for signal and spillover and (b) a zoom to see the spillover profile.

6.4 Tracking

The effect of the added noise on the tracking efficiencies, ghost rate and timing for the different tracking algorithms (forward [2] and seed [3]) are shown in Fig. 18 and Tab. 19. The performance of the tracking depends critically on the temperature of the SiPM's due to the dark noise. The number of thermal noise clusters starts to increase dramatically beyond $-40\,^{\circ}\mathrm{C}$. Basically increasing by a factor 4 to 5 every $10\,^{\circ}\mathrm{C}$ warmer. Furthermore, it can be seen that the ghost rate, the timing and track efficiency are acceptible up to $-30\,^{\circ}\mathrm{C}$. This temperature corresponds to 1100 additional noise clusters per event, which translates into 9 MHz of noise cluster rate per SiPM.

The dark noise rate increases with radiation dose and the default scenario corresponds to that after 10 years of nominal operation (i.e. $50\,\mathrm{fb}^{-1}$). As no safety factor is included in this study, it is clear that the operating temperature should not be chosen too close to this edge. On the other hand, by increasing the clustering thresholds, the noise rate can be reduced drastically at the cost of a (small) drop in cluster efficiency. The effect of the

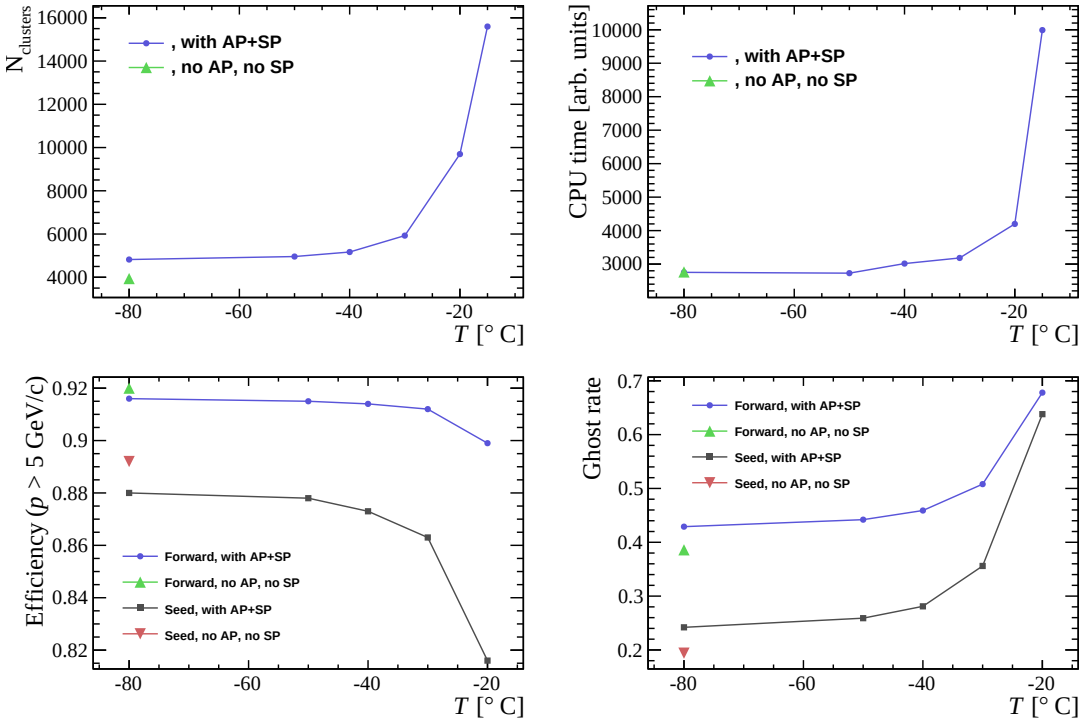

Figure 18: Effect of the thermal noise on the tracking performance, with afterpulsing (AP) and spillover (SP), and without AP and SP. 100 events were used for the Nclusters and timing plots, while 1200 events were used for the efficiency and ghost rate.

(100 evt) with AP+SP	T (C)	-15	-20	-30	-40	-50	-273
	Nclusters	15595,85	9696,56	5927,33	5168,4	4959,02	4820,81
	Timing Reco seq.	9989	4199	3183	3015,08	2729,24	2752,6
	Forward ghosts / tracks	0,852189059	0,67051198	0,4947331	0,4505053	0,4337534	0,4209061
	Forward long > 5 GeV Reco/Able	0,882081565	0,90791659	0,928031	0,9278465	0,9295073	0,9324599
	Seed ghosts / tracks	0,858841029	0,60724872	0,3385467	0,2704849	0,2510499	0,2331336
	Seed long >5GeV Reco/Able	0,917696992	0,94740727	0,9667835	0,9719505	0,9710279	0,971766
(100 evt) no AP+SP	T (C)	-15	-20	-30	-40	-50	-273
	Nclusters						3941,28
	Timing Reco seq.						2765
	Forward ghosts / tracks						0,3655811
	Forward long > 5 GeV Reco/Able						0,935966
	Seed ghosts / tracks						0,1523667
	Seed long >5GeV Reco/Able						0,976933

Figure 19: Table of datapoints used in Fig. 18: Effect of the thermal noise on the tracking performance, with afterpulsing (AP) and spillover and without afterpulsing and spillover. Timing is in arbitrary units. Note that these numbers are obtained using 100 events.

clustering thresholds will be studied later.

7 Conclusion

The main digitisation effects of the fibre detector are described in the simulation for the LHCb upgrade. This comprises the attenuation of the fibres after irradiation, the geometry of the fibres with respect to the SiPM channels, the gain of the SiPM's, the thermal noise, the noise from afterpulses and spillover, and the clustering are described. The clustering thresholds result in a high cluster efficiency of $\sim 99\%$. Afterpulses and spillover increase the number of cluster by, respectively, 11% and 10%. The thermal noise give the largest contribution to the noise rate after 10 years of operation when operating at $T \gtrsim -30\,^{\circ}\mathrm{C}$. For every $10\,^{\circ}\mathrm{C}$ warmer, the dark noise rate is expected to increase dramatically by a factor $4 - 5$. The tracking performance remains good up to $-30\,^{\circ}\mathrm{C}$, corresponding to 9 MHz of noise cluster rate per SiPM. The tracking performance decreases drastically when increasing the temperature. The effect of the clustering thresholds on the cluster efficiency and noise still has to be studied seperately.

References

[1] L. del Buono *et al.*, *Geometry of the scintillating fiber detector*, CERN-LHCb-PUB-2014-005.

[2] Y. Amhis *et al.*, *Description and performance studies of the forward tracking algorithm for a scintillating fibre detector at lhcb*, CERN-LHCb-PUB-2014-001.

[3] Y. Amhis *et al.*, *The seeding tracking algorithm for a scintillating fibre detector at lhcb*, CERN-LHCb-PUB-2014-002.

[4] Geant4 collaboration, S. Agostinelli *et al.*, *Geant4: a simulation toolkit*, Nucl. Instrum. Meth. **A506** (2003) 250.

[5] Geant4 collaboration, J. Allison *et al.*, *Geant4 developments and applications*, IEEE Trans. Nucl. Sci. **53** (2006) 270.

[6] M. Deckenhoff, PhD thesis, Technische Universität Dortmund, 2014, to be published.

[7] P. Moreira *et al.*, *The GBT, a proposed architecture for multi-Gb/s data transmission in high energy physics*, proceedings of the Topical Workshop on Electronics for Particle Physics TWEPP-07, CERN-2007-07 (2007), p. 332-336.